SUPPORTING INFORMATION

Thickness-dependent perovskite octahedral distortions at heterointerfaces

Jennifer Fowlie[§], Céline Lichtensteiger[§], Marta Gibert[§†], Hugo Meley[§], Philip Willmott[‡⊥] and Jean-Marc Triscone[§]*

[§]Department of Quantum Matter Physics, University of Geneva, 24 Quai Ernest-Ansermet, 1211 Geneva, Switzerland

[‡] Swiss Light Source, Paul Scherrer Institut, 5232 Villigen PSI, Switzerland

[⊥] Physik Institut, University of Zürich, 190 Winterthurerstrasse, 8057 Zürich, Switzerland

* Correspondence to jennifer.fowlie@unige.ch, phone +41 (0) 22 379 3729

I. FILM GROWTH AND CHARACTERIZATION

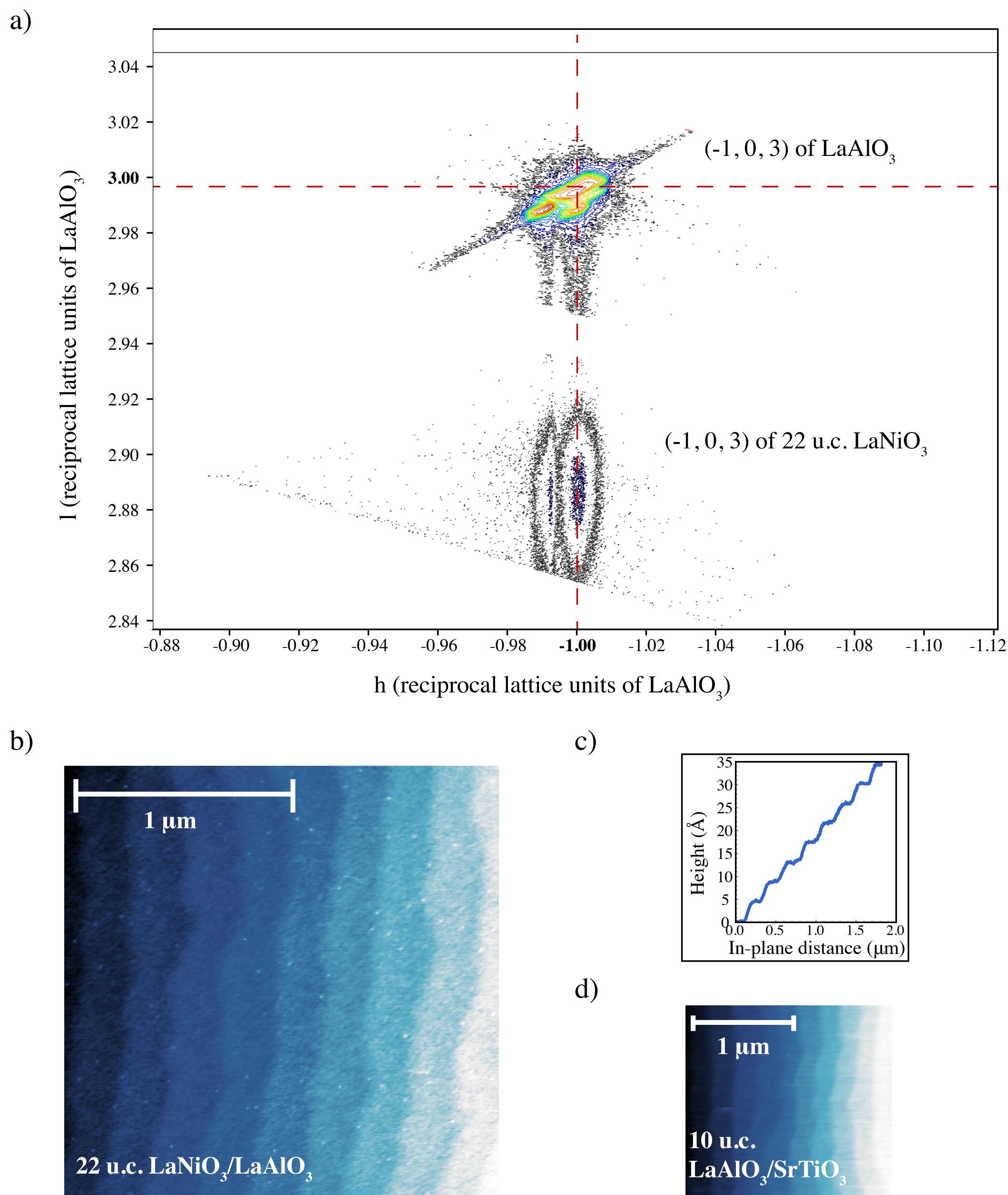

Figure S1. a) A (non-synchrotron source) reciprocal space map around a non-specular reflection of a $LaNiO_3$ film 22 u.c. in thickness on a (001)-oriented $LaAlO_3$ substrate. The red dashed lines mark the coordinates of maximum intensity. b) The atomic force microscopy topography of the

same 22 u.c. $LaNiO_3$/ $LaAlO_3$ showing the step terraces. c) The horizontal height profile of the topography in b) illustrating that the step height equates to single unit cells. d) The topography of the 10 u.c. $LaAlO_3/SrTiO_3$ sample analyzed in detail as part of this work.

All samples reported on were extensively characterized. Figure S1 shows some typical characterization for a 22 u.c. $LaNiO_3$ film grown on a $(001)_{pc}$-oriented $LaAlO_3$ substrate from the same series as the samples discussed in the main text. Panel a) contains a reciprocal space map recorded in-house around the (-1, 0, 3) Bragg reflection. The rhombohedral twinning of the substrate is seen by the multi-peaked nature of the reflection and this is clearly imprinted into the film. The alignment in h of the substrate and film peak indicates that the film lattice parameter remains fixed to that of the substrate by, in this case compressive, epitaxial strain. Panel b) is the film topography and c) is the horizontal profile of this topography. Panel d) shows a topography for the 10 u.c. $LaAlO_3/SrTiO_3$ film for which the HIBPs were measured in this work. Both topographies reproduce the step-terrace structure of the substrates faithfully while the unit cell steps of the profile confirm the single-site termination.

Figure S2 shows the specular CTRs recorded at synchrotron for the series of $LaNiO_3$ films reported in the main text. The total sample thickness was extracted from these scans by means of comparison with a simulation [1].

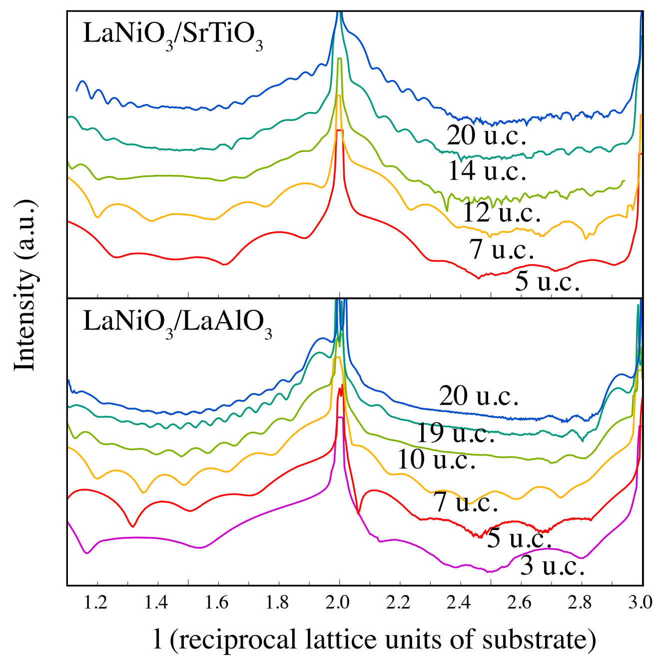

Figure S2. The specular CTRs for all the $LaNiO_3$ samples analyzed in the main text plus some thicknesses not analyzed.

II. GEOMETRIC CONSIDERATIONS

The procedure for generating atomic positions for the oxygen octahedra of a perovskite is described briefly in the main text. Here more details are added as well as justification for the steps undertaken.

The main assumption made in this procedure is that the octahedra are perfectly rigid, although, in reality, some degree of bond length distortion is expected. Because we are considering the rotation of a rigid body, it is important that the rotation angles (α, β and γ) are taken with respect to the internal symmetry axes of the octahedron (imaginary lines connecting opposing oxygen atoms) and not to the original, unrotated Cartesian axes. Figure S3 illustrates how the axes are defined and redefined for an order of operation of the Glazer angles $\alpha \rightarrow \beta \rightarrow \gamma$.

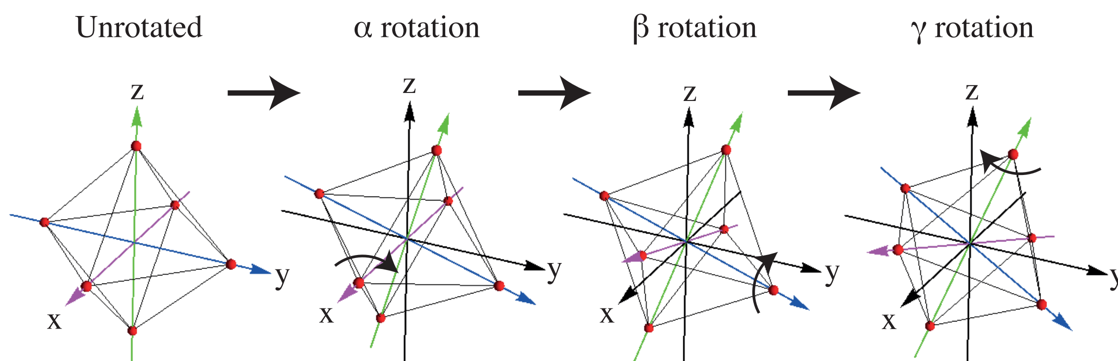

Figure S3. Schematic to show how the axes of rotation are defined with respect to the unrotated Cartesian axes (in black). α rotations are around what started as the Cartesian x-axis (magenta), β rotations are around the former y-axis (blue) and γ rotations are around what used to be the z-axis (green) but has now been rotated by the previous operations. After each partial rotation the axes are redefined.

A second geometric subtlety is that the group of 3-dimensional rotations, SO(3), is non-Abelian, meaning that the order in which the rotations are applied will change the final atomic positions. We find that for small angles of distortion, less than 10°, the variation between the final vectors is minimal and the rotations could be performed in any order for a very similar result. When the rotation magnitude exceeds 10°, however, the final positions begin to diverge heavily with a change in the order of operation. A way to get around this issue is to break the large rotation angle operation into several small rotation angle operations.

The operation is performed by the Rodrigues formula [2] for a three dimensional rotation, φ, around a general vector, (u_x, u_y, u_z):

$$\begin{pmatrix} cos\varphi + u_x^2(1 - cos\varphi) & u_y u_x(1 - cos\varphi) - u_z sin\varphi & u_z u_x(1 - cos\varphi) + u_y sin\varphi \\ u_x u_y(1 - cos\varphi) + u_z sin\varphi & cos\varphi + u_y^2(1 - cos\varphi) & u_z u_y(1 - cos\varphi) - u_x sin\varphi \\ u_x u_z(1 - cos\varphi) - u_y sin\varphi & u_y u_z(1 - cos\varphi) + u_x sin\varphi & cos\varphi + u_z^2(1 - cos\varphi) \end{pmatrix}$$

For our purposes, the Rodrigues formula is applied iteratively around the three internal axes of octahedral symmetry in turn, each time by an increment of the total rotation angle for that axis. The mth incremental rotation, φ, is performed around a unique vector $(u_x, u_y, u_z)_m$, which has been defined by successive application of all the m-1 rotation operations before. To obtain a final set of vectors that is independent upon the order of operation, 50 iterations of the Rodrigues formula around each axis is found to be sufficient for a convergence within 0.1 % when the Glazer rotation magnitudes are very large (more than 15°, in reality the magnitudes tend to be less than 15°). Figure S4 shows how the resulting atomic positions, which depend upon the order of operation, converge to the same vector coordinates when the number of iterations increases.

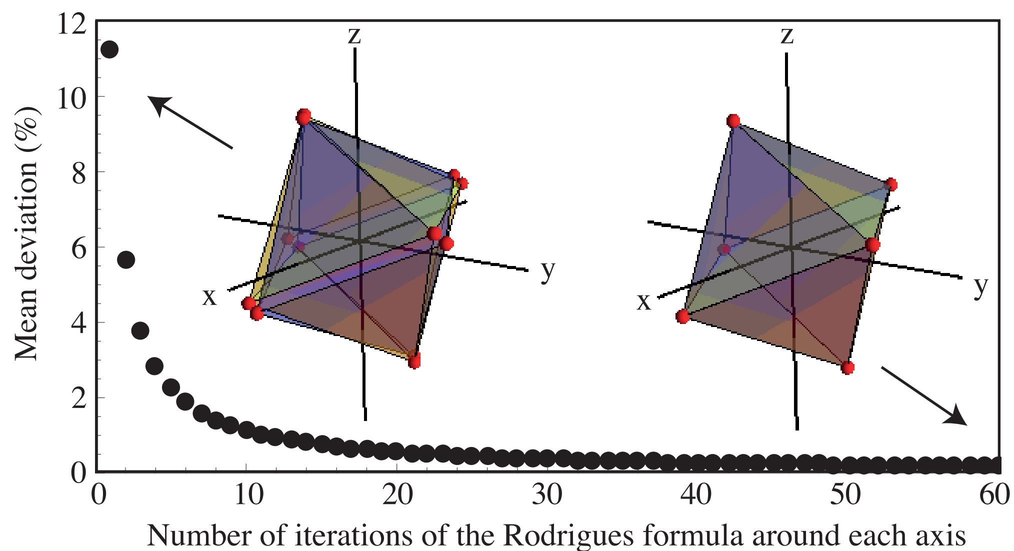

Figure S4. The percentage mean difference between resulting vectors defining the atomic positions calculated with the rotations applied in the order α → β → γ compared to in the order γ → β → α. The insets are the graphical outputs of the simulation when the angles are applied in their entirety (one iteration) and when there are 60 iterations, each time by $\frac{\alpha}{60}, \frac{\beta}{60}$ and $\frac{\gamma}{60}$. Note that the angles for this demonstration were very large; α = β = 16° and γ = 17°.

III. MEASURED AND FITTED HALF-INTEGER BRAGG PEAK

The experimental intensity is taken to be the integrated intensity under the peak corresponding to diffraction from the film alone. The full fit is the sum of a pseudo-Voigt profile for the substrate, a Gaussian function for the film, a linear slope offset and a constant background. The result of this fit for an example peak is shown in Figure S5. Considering only the Gaussian part of the film, the integrated intensity is then the area under this function.

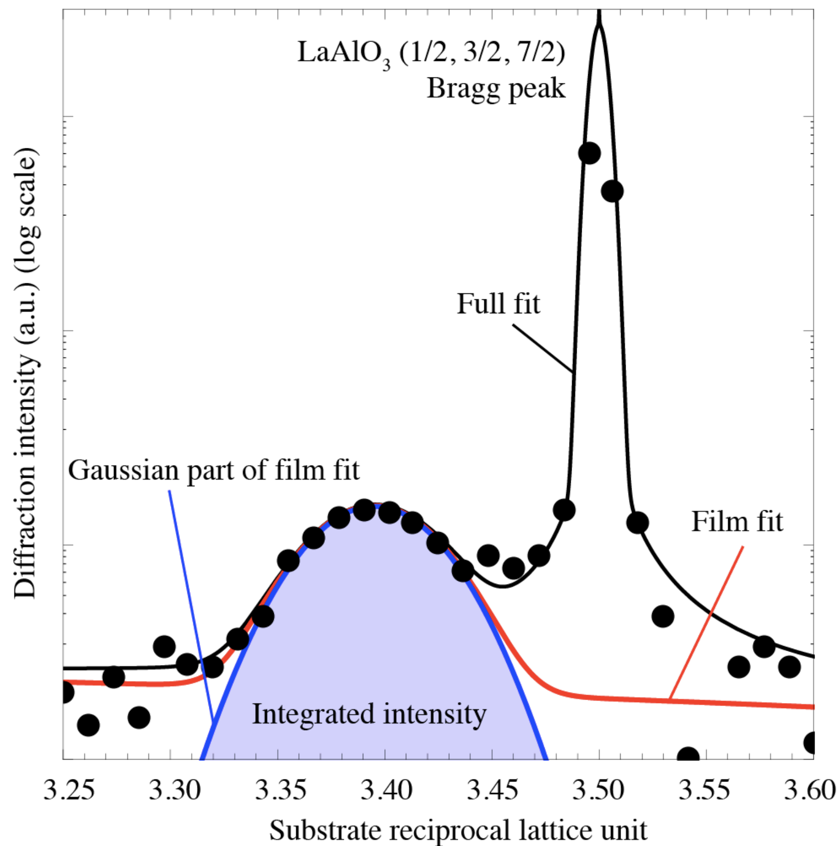

Figure S5. An example of a low intensity HIBP, $(\frac{1}{2},\frac{3}{2},\frac{7}{2})$, of the $LaAlO_3$ substrate and a 20 u.c. $LaNiO_3$ film. Fits to the full diffractogram and the film contribution are shown in black and red respectively as well as the Gaussian part of the film contribution from which the integrated intensity is found.

IV. COHERENCE THICKNESS OF OCTAHEDRAL DISTORTIONS

As described in the previous supplementary section, the HIBPs can be fitted with a Gaussian function. The full width at half maximum of this peak is directly related to the thickness of the structure that gives rise to it. This “coherence” thickness is given by the Scherrer formula where, in this formulation, c is the pseudocubic lattice parameter of the substrate with the dimension of length and the FWHM is expressed relative to the substrate reciprocal lattice units:

$$t_{coherence} = \frac{c}{FWHM(r.l.u)}$$

We have calculated this quantity for all the thicknesses of $LaNiO_3$ on both substrates, using the mean of the FWHM values for all the HIBPs and plotted this as a function of total film thickness, as determined from the finite thickness effect of the specular CTRs in Figure S6. The error bars correspond to the standard deviation on the mean of FWHMs of the series of HIBPs.

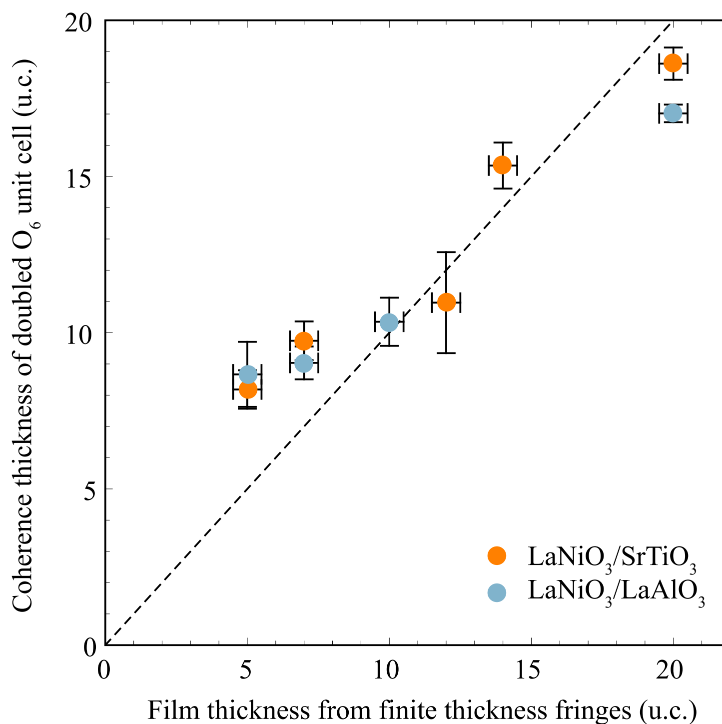

Figure S6. The coherence thickness of the distorted oxygen octahedral network as a function of the film thickness as determined by the finite thickness effect. The dashed line shows the 1:1 relationship.

As can be seen in Figure S6, the O_6 network distortion essentially occupies the entire film thickness. The only significant deviation from the 1:1 relationship with the total film thickness occurring in the thinnest films. There is a suggestion that the octahedral distortion extends around 2 u.c. further than the film itself, possibly indicating an influence into the substrate.

V. COMPARISON OF EXPERIMENTAL AND SIMULATED INTENSITIES

As described in the main text, for all the half-integer Bragg peaks (HIBPs) measured, the same (h, k, l) must be simulated over the parameter space defined by α (= β) and γ (with the domain populations as well for certain systems). Then, at each point in parameter space, the residual sum of squares (RSS) is calculated as a quantification of how well the simulated diffraction intensities match the measured ones for that combination of input Glazer angles.

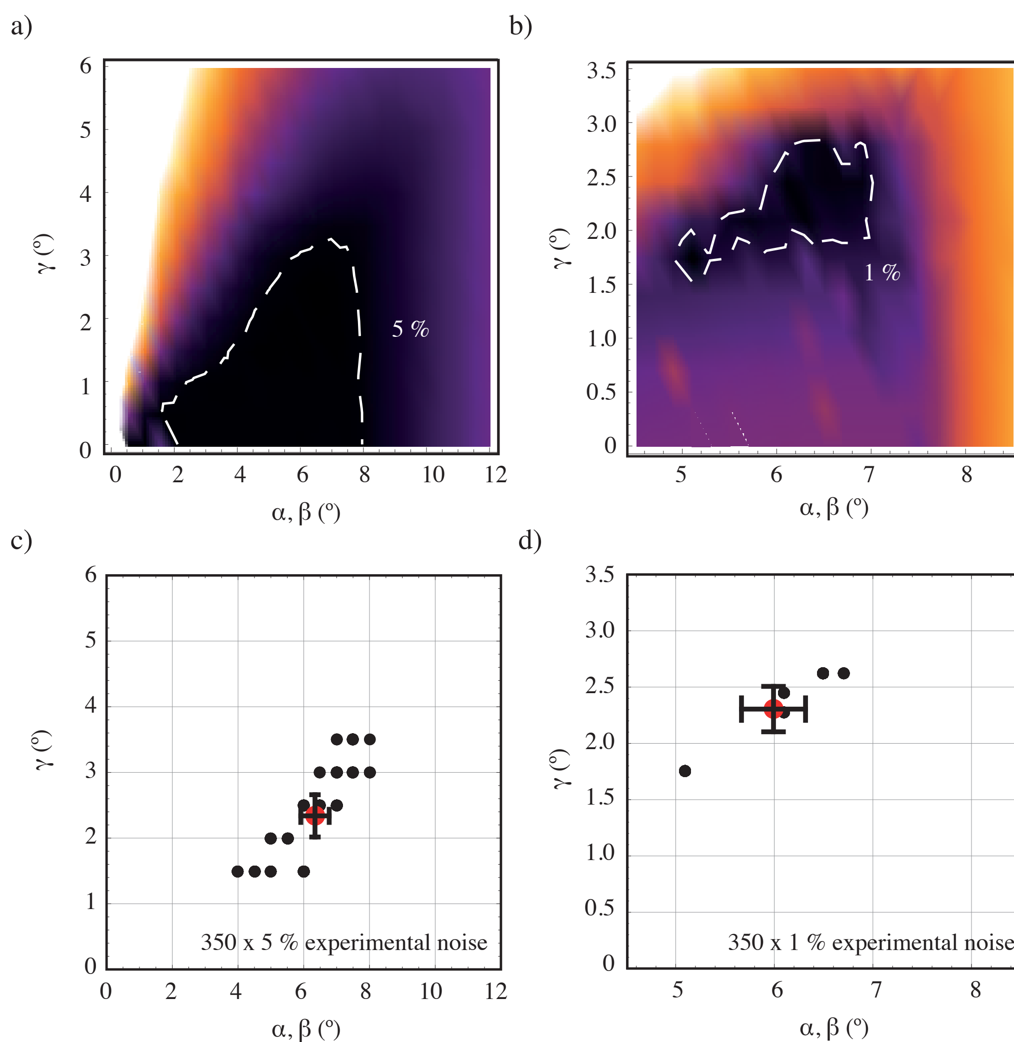

Figure S7. a) and b) are density plots in the parameter space of the input Glazer angles showing

the RSS of the optimisation. The darker color indicates a lower residual and, hence, a better fit. Shown by the dashed white line is the contour marking the values where the residual corresponds to 5 % (a) and 1 % (b) of its minimum. c) and d) are scatter plots showing the values of α (=β) and γ that produce the lowest RSS, in other words the best fit, when the process is repeated 350 times with a random noise added to the experimental data that is within 5 % (c) and 1 % (d). The mean of the 350 runs (all the black points, many of which are superimposed) is shown by the red mark and the error bars correspond to the standard deviation on this mean.

Figure S7 shows the output of the simulation for a (001)-oriented $LaAlO_3$ film of 10 u.c. thickness grown on a $SrTiO_3$ substrate. Panels a) and b) are density plots of the RSS. Panel b) is calculated with a higher level of precision in the parameter space. Panels c) and d) show the input angles that give the lowest RSS values when the optimisation is repeated hundreds of times, each time with a random noise of ± 5 % (c) and ± 1 % (d). The optimised α, β and γ remain within the same range of values with the application of artificial experimental noise, indicating the robustness of the simulation to the input data. This demonstrates that the simulation is not overfitting and this approach has been used in other, similar, studies [3]. The following expression describes how, for each measured intensity I_{exp}, a new intensity with added noise, I'_{exp} can be generated:

$$I'_{exp}(h,k,l)_n = I_{exp}(h,k,l)_n + R_n I_{exp}(h,k,l)_n$$

In this process, the parameter R_n is a randomly generated number between, for instance, –0.05 and +0.05 for a 5 % artificial error.

Over 350 repetitions give a mean of $\alpha = \beta = 6^{\circ}$ and $\gamma = 2.3^{\circ}$ (panel d)), which corresponds to the

minimum RSS in the density plot (panel b)) and all the scattered values coming from the artificially-added experimental noise lie within the contour delineating 1 % of the minimum RSS. Therefore the mean of the scattered data is taken as the final result and the same procedure is carried out to obtain the Glazer tilt and rotation magnitudes for all other samples reported in the main text.

Figure S8 shows a comparison of the measured and simulated diffraction intensities given the best-fit angles for the 5 u.c. $LaNiO_3/SrTiO_3$ film. The normalization was done with respect to the $\left(\frac{1}{2},\frac{3}{2},\frac{1}{2}\right)$ peak.

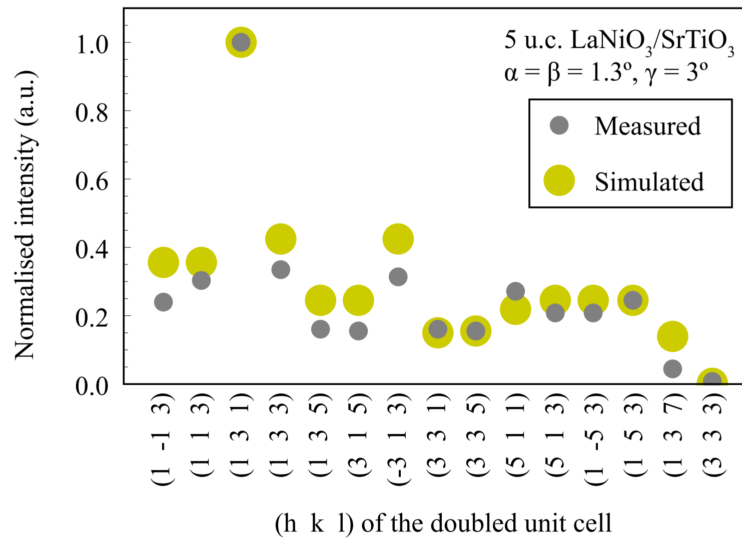

Figure S8. Measured HIBP intensities compared to the simulated intensities given the determined best-fit parameters.

Table S1 contains these results, which correspond to Figure 4.

Table S1. Summary of the structural parameters obtained from the synchrotron XRD

Heterostructure	Thickness	c-axis parameter	$\alpha = \beta$	γ
$LaAlO_3/SrTiO_3$	10 u.c.	3.73 Å	6.0°	2.3°
$LaAlO_3/SrTiO_3$	5 u.c.	3.73 Å	0.7°	0.2°
$LaNiO_3/SrTiO_3$	20 u.c.	3.81 Å	8.8°	0.0°
$LaNiO_3/SrTiO_3$	14 u.c.	3.80 Å	8.8°	0.0°
$LaNiO_3/SrTiO_3$	12 u.c.	3.80 Å	6.0°	0.0°
$LaNiO_3/SrTiO_3$	7 u.c.	3.73 Å	2.8°	3.0°
$LaNiO_3/SrTiO_3$	5 u.c.	3.72 Å	1.3°	3.0°
$LaNiO_3/ LaAlO_3$	20 u.c.	3.92 Å	1.7°	10.0°
$LaNiO_3/ LaAlO_3$	10 u.c.	3.92 Å	1.7°	11.0°
$LaNiO_3/ LaAlO_3$	7 u.c.	3.92 Å	1.8°	10.0°
$LaNiO_3/ LaAlO_3$	5 u.c.	3.92 Å	0.4°	9.5°

VI. OTHER STRUCTURAL PARAMETERS

As we have successfully determined the octahedral tilt and rotation angles as well as the c-axis lattice parameter, and the a- and b-axis lattice parameters are imposed by the substrate, we can calculate the resulting Ni-O-Ni bond angles and Ni-O bond lengths for all the $LaNiO_3$ films.

These parameters are plotted in Figure S9.

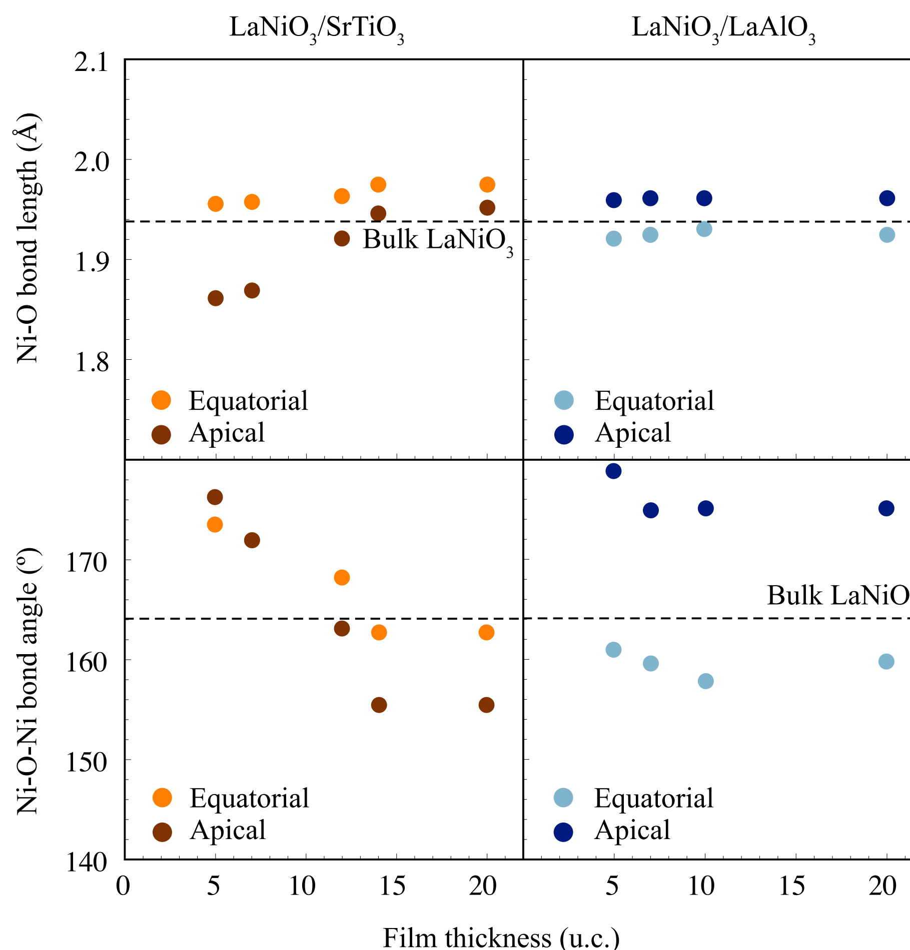

Figure S9. The Ni-O-Ni bond angle and Ni-O bond lengths in both equatorial and apical directions as a function of thickness for the two series of $LaNiO_3$ films on different substrates. The dashed lines indicate the relevant parameter in bulk $LaNiO_3$.

REFERENCES

(1) Lichtensteiger, C. *InteractiveXRDFit*: A New Tool to Simulate and Fit X-Ray Diffractograms of Oxide Thin Films and Heterostructures. *J. Appl. Crystallogr.* **2018**, *51* (6), 1–7. https://doi.org/10.1107/S1600576718012840.

(2) Rodrigues, O. Des Lois Géometriques Qui Regissent Les Déplacements d' Un Systéme Solide Dans l' Espace, et de La Variation Des Coordonnées Provenant de Ces Déplacement Considérées Indépendant Des Causes Qui Peuvent Les Produire. *J. Math. Pures. Appl.* **1840**, *5*, 380–440.

(3) Brahlek, M.; Choquette, A. K.; Smith, C. R.; Engel-Herbert, R.; May, S. J. Structural Refinement of Pbnm -Type Perovskite Films from Analysis of Half-Order Diffraction Peaks. *J. Appl. Phys.* **2017**, *121* (4). https://doi.org/10.1063/1.4974362.